

An Efficient Closed-Form Solution to Full Visual-Inertial State Initialization

Samuel Cerezo¹, Seong Hun Lee¹, Javier Civera¹

Abstract—In this letter, we present a closed-form initialization method that recovers the full visual–inertial state without nonlinear optimization. Unlike previous approaches that rely on iterative solvers, our formulation yields analytical, easy-to-implement, and numerically stable solutions for reliable start-up. Our method builds on small-rotation and constant-velocity approximations, which keep the formulation compact while preserving the essential coupling between motion and inertial measurements. We further propose an observability-driven, two-stage initialization scheme that balances accuracy with initialization latency. Extensive experiments on the EuRoC dataset validate our assumptions: our method achieves 10–20% lower initialization error than optimization-based approaches, while using 4× shorter initialization windows and reducing computational cost by 5×.

I. INTRODUCTION

Visual–inertial SLAM has become a core technology in robotics and mobile devices, enabling real-time localization and mapping by fusing camera and inertial measurements [1], [2], [3]. While camera intrinsics can be calibrated once and remain relatively stable over time, inertial sensors must be re-initialized at each run. This initialization step estimates critical quantities such as the initial velocity, gravity direction, and gyroscope and accelerometer biases, which serve as the seed for subsequent state estimation. Accurate initialization is therefore essential: poor initial estimates may cause optimization or filtering to converge to local minima, leading to scale drift, degraded tracking, or even complete failure of the system. Conversely, proper initialization enhances robustness under challenging conditions and recovers the metric scale that monocular vision alone cannot provide.

A central insight from the SLAM literature is that orientation plays a pivotal role: once rotations are reliably estimated, the recovery of the remaining states becomes substantially more robust. Carlone and Censi [4] showed that accurate orientation estimation prevents spurious minima in pose-graph optimization, and Carlone et al. [5] showed that good rotation initialization significantly improves convergence and accuracy in large-scale SLAM. These results motivate our approach, which relies on simple but accurate orientation approximations to estimate the rest of the states.

Existing visual–inertial initialization strategies fall into two main categories. Closed-form solutions have been proposed by Martinelli [6], [7], but they assume partial knowledge of the states, specifically of the sensor biases. Later works addressed this limitation using iterative nonlinear

optimization [8], [9], [10], [11], which achieves accurate full state initialization but requires careful seeding and incurs significant computational cost. More recent formulations attempt to reduce complexity by decoupling rotation and translation [12], [13], [14], or by combining closed-form solutions with filtering schemes [15]. However, none of these approaches provides a fully analytical solution for the complete visual–inertial state.

In this letter, we present the first closed-form initialization method that simultaneously estimates all states of a visual–inertial system, including gyroscope and accelerometer biases. Our formulation builds upon the small-rotation and constant-velocity approximations, which hold for common sensor hardware and motion patterns. We further contribute a two-stage criterion that assesses the observability of the visual–inertial states and enables reliable initialization under diverse conditions. Extensive experiments show that our method achieves higher accuracy than optimization-based baselines while significantly reducing the computational cost and initialization delay.

II. RELATED WORK

Early works on closed-form initialization were introduced by Martinelli [6], [7], who derived minimal unique solutions under the assumption of known gyroscope and accelerometer biases. Subsequent approaches shifted towards nonlinear optimization to jointly estimate these biases together with the remaining states [8], [9], and later refinements such as those by Campos et al. [10], [11] achieved robust results but still relied on iterative procedures requiring careful seeding.

More recently, alternative formulations have been proposed to improve efficiency and robustness. Evangelidis and Mícušík [16] revisited the problem with a new closed-form solver for the vi-SfM problem, elegant but better suited for offline reconstruction. Decoupled approaches to relative [17] and multi-view [12] camera motion have also been proposed [13], [14], but they still require nonlinear optimization and in some cases cannot recover accelerometer bias. Hybrid strategies such as the framework of Wang et al. [15] can estimate both biases through an error-state Kalman filter, at the expense of additional algorithmic complexity.

In parallel, approximations have played an important role in related problems: the small-angle approximation in triangulation [18], [19], and the small-rotation approximation in vision-only reconstruction from accidental motion [20] and efficient relative pose solvers [21]. However, to the best of our knowledge, the small-rotation approximation has never been exploited for visual-inertial state initialization.

¹The authors are with School of Engineering and Architecture, Universidad de Zaragoza, 50018, Zaragoza, Spain {sacerezo, seonghunlee, jcivera}@unizar.es

Method	Closed-form	Gyro-bias	Accel-bias
Martinelli [7]	✓	✗	✗
Kaiser et al. [8]	✗	✓	✓
Domínguez et al. [9]	✗	✓	✓
Campos et al. [10], [11]	✗	✓	✓
Concha et al. [13]	✗	✓	✓
Evangelidis and Micušik [16]	✓	✗	✗
Wang et al. [15]	✗	✓	✓
Ours	✓	✓	✓

TABLE I: **Comparison of existing initialization methods.** Summary of whether each method provides a closed-form solution and estimates gyroscope and accelerometer biases.

In summary, existing methods either assume known biases, rely on iterative optimization, or adopt hybrid formulations that increase complexity. In contrast, we propose a full-state closed-form solution by only assuming small rotations—a reasonable condition for typical hardware and most use cases. Our approach therefore combines the accuracy of optimization-based methods with the simplicity and efficiency of analytical solvers.

III. NOTATION AND PRELIMINARIES

Vectors are denoted by bold lowercase letters (\mathbf{x}), with unit vectors indicated by a hat accent ($\hat{\mathbf{x}}$). Bold upper-case letters (\mathbf{A}) represent matrices, and light lower-case letters (a) denote scalars. Rotation matrices $\mathbf{R}_{ab} \in \text{SO}(3)$ refer to the transformation from frame b to frame a , omitting the first subindex when referring to the world frame w , *i.e.*, $\mathbf{R}_a \doteq \mathbf{R}_{wa}$. In axis-angle form, $\mathbf{r} = \theta \hat{\mathbf{r}} \in \mathbb{R}^3$, with the unit rotation axis $\hat{\mathbf{r}} = \frac{\mathbf{r}}{\|\mathbf{r}\|} \in \mathbb{S}^2$ and the rotation angle $\theta = \|\mathbf{r}\| \in \mathbb{R}$. The skew-symmetric matrix of \mathbf{r} is denoted \mathbf{r}^\wedge . Our IMU integration between time instants t_i and t_j follows the standard formulation [22]

$$\mathbf{R}_j = \mathbf{R}_i \prod_{k=i}^{j-1} \text{Exp} \left(\left(\tilde{\omega}_k - \mathbf{b}_k^g - \boldsymbol{\eta}_k^{gd} \right) \Delta t \right), \quad (1)$$

$$\mathbf{v}_j = \mathbf{v}_i + \mathbf{g} \Delta t_{ij} + \sum_{k=i}^{j-1} \mathbf{R}_k \left(\tilde{\mathbf{a}}_k - \mathbf{b}_k^a - \boldsymbol{\eta}_k^{ad} \right) \Delta t \quad (2)$$

$$\mathbf{t}_j = \mathbf{t}_i + \sum_{k=i}^{j-1} \left[\mathbf{v}_k \Delta t + \frac{1}{2} \mathbf{g} \Delta t^2 + \frac{1}{2} \mathbf{R}_k \left(\tilde{\mathbf{a}}_k - \mathbf{b}_k^a - \boldsymbol{\eta}_k^{ad} \right) \Delta t^2 \right] \quad (3)$$

where \mathbf{v}_i and \mathbf{v}_j denote the linear velocity at times t_i and t_j , \mathbf{g} the gravity vector and Δt the sampling interval between consecutive IMU measurements. $\tilde{\omega}_k$ and $\tilde{\mathbf{a}}_k$ are the gyroscope and accelerometer readings at time k , with associated biases \mathbf{b}_k^g and \mathbf{b}_k^a , respectively. We assume that gyroscope and accelerometer biases remain approximately constant during initialization, *i.e.*, $\mathbf{b}_k^g \approx \mathbf{b}^g$ and $\mathbf{b}_k^a \approx \mathbf{b}^a$. We denote the number of preintegrated IMU measurements by $L = j - i - 1$, and hence $t_j - t_i = L \Delta t$.

IV. ROTATION AND GYRO BIAS INITIALIZATION

For a small ($\theta \rightarrow 0$) rotation vector \mathbf{r} , the Rodrigues' formula relates it to a rotation matrix representation as

$$\mathbf{R} = \mathbf{I}_3 + \frac{\sin \theta}{\theta} \mathbf{r}^\wedge + \frac{1 - \cos \theta}{\theta^2} \mathbf{r}^\wedge{}^2 \underset{\theta \rightarrow 0}{\approx} \mathbf{I}_3 + \mathbf{r}^\wedge, \quad (4)$$

where \mathbf{I}_3 is the 3×3 identity matrix. Notably, under this approximation, rotation matrices commute only up to second-order terms. Approximating $\mathbf{R}_{ab} \approx \mathbf{I} + \mathbf{r}_{ab}^\wedge$ and $\mathbf{R}_{cd} \approx \mathbf{I} + \mathbf{r}_{cd}^\wedge$, the products $\mathbf{R}_{ab} \mathbf{R}_{cd}$ and $\mathbf{R}_{cd} \mathbf{R}_{ab}$ then become

$$\mathbf{R}_{ab} \mathbf{R}_{cd} \approx \mathbf{I} + \mathbf{r}_{ab}^\wedge + \mathbf{r}_{cd}^\wedge + \cancel{\mathbf{r}_{ab}^\wedge \mathbf{r}_{cd}^\wedge} \quad (5)$$

$$\mathbf{R}_{cd} \mathbf{R}_{ab} \approx \mathbf{I} + \mathbf{r}_{cd}^\wedge + \mathbf{r}_{ab}^\wedge + \cancel{\mathbf{r}_{cd}^\wedge \mathbf{r}_{ab}^\wedge} \quad (6)$$

differing only in the neglected second-order cross products of the skew-symmetric matrices $\mathbf{r}_{ab}^\wedge \mathbf{r}_{cd}^\wedge$ and $\mathbf{r}_{cd}^\wedge \mathbf{r}_{ab}^\wedge$, which generally do not commute¹. However, under the small-rotation assumption, these second-order contributions are negligible relative to the first-order terms, making the two matrix products approximately equal.

Rodrigues' formula also provides the exponential map $\text{Exp} : \mathfrak{so}(3) \rightarrow \text{SO}(3)$. For small rotation vectors \mathbf{r}_{ab} and \mathbf{r}_{cd} , the exponential of their sum approximates the product of exponentials:

$$\begin{aligned} \text{Exp}(\mathbf{r}_{ab} + \mathbf{r}_{cd}) &\underset{\theta \rightarrow 0}{\approx} \mathbf{I}_3 + (\mathbf{r}_{ab} + \mathbf{r}_{cd})^\wedge = \mathbf{I}_3 + \mathbf{r}_{ab}^\wedge + \mathbf{r}_{cd}^\wedge \\ &= (\mathbf{I}_3 + \mathbf{r}_{ab}^\wedge) (\mathbf{I}_3 + \mathbf{r}_{cd}^\wedge) = \text{Exp}(\mathbf{r}_{ab}) \text{Exp}(\mathbf{r}_{cd}) \end{aligned} \quad (7)$$

With this, the exponential maps in Eq. (1) can be decomposed into products as shown below

$$\prod_{k=i}^{j-1} \text{Exp}((\tilde{\omega}_k - \mathbf{b}^g) \Delta t) \underset{\theta \rightarrow 0}{\approx} \prod_{k=i}^{j-1} \text{Exp}(\tilde{\omega}_k \Delta t) \text{Exp}(-\mathbf{b}^g \Delta t) \quad (8)$$

By first commuting the products of the right part, and then applying Eq. (7), we obtain the following expression

$$\mathbf{R}_{ij} = \mathbf{R}_i^\top \mathbf{R}_j \underset{\theta \rightarrow 0}{\approx} \prod_{k=i}^{j-1} (\text{Exp}(\tilde{\omega}_k \Delta t) \text{Exp}(-\mathbf{b}^g \Delta t)) \quad (9)$$

$$\underset{\theta \rightarrow 0}{\approx} \prod_{k=i}^{j-1} (\text{Exp}(\tilde{\omega}_k \Delta t)) \prod_{k=i}^{j-1} (\text{Exp}(-\mathbf{b}^g \Delta t)) \quad (10)$$

$$= \prod_{k=i}^{j-1} (\text{Exp}(\tilde{\omega}_k \Delta t)) \text{Exp}(-L \mathbf{b}^g \Delta t) \quad (11)$$

from which \mathbf{b}^g can be solved analytically. This yields our first closed-form solution, referred to as **commutative approximation**

\mathbf{b}^g using the commutative approximation

$$\mathbf{b}^g \approx -\frac{1}{L \Delta t} \text{Log} \left(\left(\prod_{k=i}^{j-1} \text{Exp}(\tilde{\omega}_k \Delta t) \right)^\top \mathbf{R}_{ij} \right) \quad (12)$$

We can derive more efficient closed-form solutions for \mathbf{b}^g by assuming constant rotation angles within each IMU

¹Skew-symmetric matrices actually commute with their adjoints.

integration. First, we express the left-hand side of Eq. (9) as the composition of L identical rotations:

$$\mathbf{R}_{ij} = \prod_{k=i}^{j-1} \text{Exp}\left(\frac{\text{Log}(\mathbf{R}_{ij})}{L}\right) \underset{\theta \rightarrow 0}{\approx} \prod_{k=i}^{j-1} (\text{Exp}(\tilde{\omega}_k \Delta t) \text{Exp}(-\mathbf{b}^g \Delta t)) \quad (13)$$

Now, suppose that $\tilde{\omega}_k$ remains approximately constant within the time interval between two images. Approximating $\tilde{\omega}_k$ in Eq. (13) by their average $\bar{\omega}_k$ and dividing both sides of the equation by L identical rotations, we get

$$\text{Exp}\left(\frac{\text{Log}(\mathbf{R}_{ij})}{L}\right) \approx \text{Exp}(\bar{\omega}_k \Delta t) \text{Exp}(-\mathbf{b}^g \Delta t), \quad (14)$$

from which we can also solve for \mathbf{b}^g analytically. We can compute $\bar{\omega}_k$ by integrating all IMU measurements or by just averaging them arithmetically, which will give us two closed-form solutions that we will denote as **average approximation** and **arithmetic average approximation** respectively.

\mathbf{b}^g using the average approximation

$$\mathbf{b}^g \approx -\frac{1}{\Delta t} \text{Log}\left(\text{Exp}(\bar{\omega}_k \Delta t)^\top \text{Exp}\left(\frac{\text{Log}(\mathbf{R}_{ij})}{L}\right)\right)$$

with $\bar{\omega}_k \approx \frac{1}{L \Delta t} \text{Log}\left(\prod_{k=i}^{j-1} \text{Exp}(\tilde{\omega}_k \Delta t)\right)$ (15)

\mathbf{b}^g using the arithmetic average approximation

$$\mathbf{b}^g \approx -\frac{1}{\Delta t} \text{Log}\left(\text{Exp}(\bar{\omega}_k \Delta t)^\top \text{Exp}\left(\frac{\text{Log}(\mathbf{R}_{ij})}{L}\right)\right)$$

with $\bar{\omega}_k = \frac{1}{L} \sum_{k=i}^{j-1} \tilde{\omega}_k$ (16)

\mathbf{R}_{ij} can be estimated from feature correspondences between any pair of frames. However, in practice, it is both feasible and convenient to initialize \mathbf{R}_{ij} and \mathbf{b}^g using only the first two frames. First, estimation errors tend to grow over time. Inertial drift accumulates, and our approximations become less accurate as more IMU readings are involved. Second, unlike translation estimates, relative rotation estimates do not necessarily benefit from larger inter-frame motions. In fact, large motions often introduce perspective distortions in feature appearance, reducing the number of reliably tracked points and increasing matching noise [23].

V. INITIAL VELOCITY, TRANSLATION, GRAVITY AND ACCELEROMETER BIAS

A. Closed-form initialization from linear point constraints

Once \mathbf{R}_{ij} and \mathbf{b}^g are initialized, the relation between inertial measurements and image tracks can be expressed linearly. Let the sets $\mathcal{Z}_i = \{\mathbf{z}_i^1, \dots, \mathbf{z}_i^n, \dots, \mathbf{z}_i^N\}$ and $\mathcal{Z}_j = \{\mathbf{z}_j^1, \dots, \mathbf{z}_j^n, \dots, \mathbf{z}_j^N\}$ denote the image coordinates of N visual features extracted in an image at t_i and tracked up to a later image, not necessarily consecutive, taken at t_j . Assuming a pinhole camera model, every feature $\mathbf{z}_c^n \in \Omega \subset$

\mathbb{R}^2 in both images $c \in \{i, j\}$ can be backprojected to a 3D point $\mathbf{p}_c^n \in \mathbb{R}^3$ in the local camera frame as follows

$$\mathbf{p}_c^n = \lambda_c^n \mathbf{K}^{-1} \begin{bmatrix} \mathbf{z}_c^n^\top & 1 \end{bmatrix}^\top = \lambda_c^n \boldsymbol{\mu}_c^n, \quad (17)$$

where $\mathbf{K} \in \mathbb{U}\mathbb{T}^+(3)$ is the camera calibration matrix, Ω is the image domain, $\boldsymbol{\mu}_j^n \in \mathcal{S}^2$ is the normalized feature bearing and $\lambda_j^n \in \mathbb{R}$ its distance along such bearing. Following [7], a linear constraint can be derived for every feature \mathbf{z}_c^n in every pair of frames taken at t_i and t_j

$$-\frac{1}{2} \mathbf{g} (L \Delta t)^2 - \mathbf{v} L \Delta t + \boldsymbol{\Gamma}_j \mathbf{b}_a + \lambda_i^n \boldsymbol{\mu}_i^n - \lambda_j^n \boldsymbol{\mu}_j^n = \mathbf{s}_j, \quad (18)$$

where the vector \mathbf{s}_j and matrix $\boldsymbol{\Gamma}_j$ are computed by integrating the IMU measurements over the interval $[t_i, t_j]$ as

$$\mathbf{s}_j = \int_{t_i}^{t_j} (t_j - \tau) \mathbf{R}_{1\tau} \tilde{\mathbf{a}}_\tau d\tau, \quad \boldsymbol{\Gamma}_j = \int_{t_i}^{t_j} (t_j - \tau) \mathbf{R}_{i\tau} d\tau. \quad (19)$$

The rotation $\mathbf{R}_{i\tau} \in SO(3)$ comes from the IMU preintegration from time t_i up to time τ using Eq. 1. Note that \mathbf{b}^g was already initialized from the first two frames. The vector $\tilde{\mathbf{a}}_\tau$ contains the accelerometer readings. By stacking the constraints from the N tracked features from frame i to frame j , we obtain the overdetermined linear system $\boldsymbol{\Xi} \mathbf{x} = \mathbf{s}$, which yields the following least-squares problem

\mathbf{g} , \mathbf{v} , \mathbf{b}^a initialization

$$\arg \min_{\mathbf{x}} (\boldsymbol{\Xi} \mathbf{x} - \mathbf{s})^2 \rightarrow \hat{\mathbf{x}} = \mathbf{v}_{\min} \left(\boldsymbol{\Xi}^\top \boldsymbol{\Xi} \right) \quad (20)$$

which we solve via singular value decomposition (SVD), being the optimal solution $\hat{\mathbf{x}}$ the eigenvector associated to the smallest eigenvalue $\mathbf{v}_{\min} \left(\boldsymbol{\Xi}^\top \boldsymbol{\Xi} \right)$. Each row of the matrix $\boldsymbol{\Xi}$ corresponds to one instance of Eq. (18), leading to a total of $3(M-1)N$ equations and $9 + NM$ unknowns, being M the number of images considered. $\boldsymbol{\Xi}$ denotes the coefficients matrix

$$\boldsymbol{\Xi} = \begin{bmatrix} T_2 & -t_2 \mathbf{I}_3 & \boldsymbol{\Gamma}_2 & \mu_1^1 & \mathbf{0}_3 & \mathbf{0}_3 & -\mu_2^1 & \mathbf{0}_3 & \mathbf{0}_3 & \mathbf{0}_3 & \mathbf{0}_3 & \mathbf{0}_3 \\ T_2 & -t_2 \mathbf{I}_3 & \boldsymbol{\Gamma}_2 & \mathbf{0}_3 & \mu_1^2 & \mathbf{0}_3 & \mathbf{0}_3 & -\mu_2^2 & \mathbf{0}_3 & \mathbf{0}_3 & \mathbf{0}_3 & \mathbf{0}_3 \\ \vdots & \vdots \\ T_j & -t_j \mathbf{I}_3 & \boldsymbol{\Gamma}_j & \mu_1^N & \mathbf{0}_3 & \mathbf{0}_3 & \mathbf{0}_3 & \mathbf{0}_3 & -\mu_2^N & \mathbf{0}_3 & \mathbf{0}_3 & \mathbf{0}_3 \\ \vdots & \vdots \\ T_j & -t_j \mathbf{I}_3 & \boldsymbol{\Gamma}_j & \mu_1^1 & \mathbf{0}_3 & \mathbf{0}_3 & \mathbf{0}_3 & \mathbf{0}_3 & \mathbf{0}_3 & -\mu_j^1 & \mathbf{0}_3 & \mathbf{0}_3 \\ T_j & -t_j \mathbf{I}_3 & \boldsymbol{\Gamma}_j & \mathbf{0}_3 & \mu_1^2 & \mathbf{0}_3 & \mathbf{0}_3 & \mathbf{0}_3 & \mathbf{0}_3 & \mathbf{0}_3 & -\mu_j^2 & \mathbf{0}_3 \\ T_j & -t_j \mathbf{I}_3 & \boldsymbol{\Gamma}_j & \mathbf{0}_3 & \mathbf{0}_3 & \mu_1^N & \mathbf{0}_3 & \mathbf{0}_3 & \mathbf{0}_3 & \mathbf{0}_3 & \mathbf{0}_3 & -\mu_j^N \end{bmatrix},$$

with $T_j = -\frac{\Delta t^2}{2} \mathbf{I}_3$. The state \mathbf{x} to be initialized is defined as

$$\mathbf{x} = \left[\mathbf{g}^\top, \mathbf{v}^\top, \mathbf{b}^a{}^\top, \lambda_1^1, \dots, \lambda_1^N, \dots, \lambda_j^1, \dots, \lambda_j^N \right]^\top,$$

and \mathbf{s} contains the measurements obtained by Eq. (19)

$$\mathbf{s} = [\mathbf{s}_2^\top, \dots, \mathbf{s}_2^\top, \mathbf{s}_3^\top, \dots, \mathbf{s}_3^\top, \mathbf{s}_j^\top, \dots, \mathbf{s}_j^\top]^\top.$$

This yields an initialization method that initializes \mathbf{R}^{ij} and \mathbf{b}^g from just the first two frames, and the rest of the states when they become observable, as illustrated in pseudocode by the Algorithm 1. A detailed analysis of the observability criteria follows in the next subsection.

Algorithm 1 Visual-Inertial State Initialization

Require: Visual-inertial data; observability thresholds $\bar{\Delta}z_{\text{th}}, \Delta\rho_{\text{th}}$
Ensure: Visual-inertial states $\mathbf{R}_{ij}, \mathbf{b}^g, \mathbf{t}_j, \mathbf{v}_j, \mathbf{b}_a, \mathbf{g}$

```

1:  $\mathcal{Z}_i \leftarrow \text{get\_first\_image\_and\_extract\_features}()$ 
2:  $\mathcal{Z}_j \leftarrow \text{get\_next\_image\_and\_track\_features}(\mathcal{Z}_i)$ 
3:  $\{\hat{\omega}_k\}, \{\hat{\mathbf{a}}_k\} \leftarrow \text{get\_IMU\_readings}()$ 
4:  $\mathbf{R}_{ij} \leftarrow \text{get\_rotation}(\mathcal{Z}_i, \mathcal{Z}_j)$ 
5:  $\mathbf{b}^g \leftarrow \text{get\_bias}(\mathbf{R}_{ij})$  ▷ Eqs. 12,15 or 16
6:  $\text{full\_obs} \leftarrow \text{false}$ 
7: while  $\text{full\_obs} = \text{false}$  do
8:    $\text{t\_obs} \leftarrow \text{translation\_obs\_test}(\mathcal{Z}_i, \mathcal{Z}_j, \mathbf{R}_{ij}, \bar{\Delta}z_{\text{th}})$  ▷ Eq. 23
9:   if  $\text{t\_obs} = \text{true}$  then
10:      $\mathbf{s}_j \leftarrow \text{integrate\_IMU}(\{\hat{\omega}_k\}, \{\hat{\mathbf{a}}_k\}, \mathbf{b}^g)$ 
11:      $\text{full\_obs} \leftarrow \text{full\_obs\_test}(\mathcal{Z}_i, \mathcal{Z}_j, \mathbf{s}_j, \Delta\rho_{\text{th}})$  ▷ Eq. 25
12:     if  $\text{full\_obs} = \text{true}$  then
13:        $\mathbf{t}_j, \mathbf{v}_j, \mathbf{b}_a, \mathbf{g} \leftarrow \text{get\_rest\_of\_vi\_states}(\mathbf{s}_j)$  ▷ Eq. 20
14:        $\text{full\_obs} \leftarrow \text{true}$ 
15:     end if
16:   end if
17:    $\mathcal{Z}_j \leftarrow \text{get\_next\_image\_and\_track\_features}(\mathcal{Z}_i)$ 
18:    $\{\hat{\omega}_k\}, \{\hat{\mathbf{a}}_k\} \leftarrow \text{get\_IMU\_readings}()$ 
19:    $\mathbf{R}_{ij} \leftarrow \text{get\_rotation}(\mathcal{Z}_i, \mathcal{Z}_j)$ 
20: end while

```

B. Two-stages Observability Test

While camera rotation and gyroscope bias are observable from any two frames, and in practice we will initialize them from the first two in the sequence, the remaining visual-inertial states are not. Specifically, using the linear system defined in Eq. (20), the full state will only be observable and hence we will be able to initialize it when Ξ is full rank. Assessing this criterion at each frame, however, may be expensive, as the matrix Ξ grows quickly with the number of frames. Motivated by this, we will evaluate observability in two stages, that are described next.

Translation Observability Test (Stage 1): This stage assesses the average parallax in the image plane between the *first* frame at t_i and a *single* subsequent frame at t_j , advancing progressively over the image sequence until the criterion is met. Specifically, we first backproject each feature \mathbf{z}_i^n extracted at t_i and project it at t_j assuming rotation-only motion between the two camera frames

$$\hat{\mathbf{z}}_j^n = h\left(\mathbf{K}\mathbf{R}_{ij}^\top \mathbf{K}^{-1} \begin{bmatrix} \mathbf{z}_i^n^\top & 1 \end{bmatrix}^\top\right). \quad (21)$$

where $h(\cdot)$ transforms the image point parameters from homogeneous to Euclidean 2D coordinates. The parallax between times t_i and t_j will be reflected in the difference between the tracks predicted with just rotational motion $\hat{\mathbf{z}}_j^n$ and the real tracks \mathbf{z}_j^n . We aggregate the parallax of all features using their average:

$$\bar{\Delta}z_j = \frac{1}{N} \sum_{n=1}^N \|\mathbf{z}_j^n - \hat{\mathbf{z}}_j^n\|_2, \quad (22)$$

The condition to be met is expressed as

$$\bar{\Delta}z_j > \bar{\Delta}z_{\text{th}}, \quad (\text{Translation Observability Test}) \quad (23)$$

If the condition is not met, we move to the next frame and repeat the test until the threshold is satisfied.

Full Observability Test (Stage 2): This stage is triggered once the motion provides sufficient translational information, i.e., when the condition in Eq. (23) holds. Following [24], we assess numerical observability via the Hessian \mathbf{H} , as follows

$$\mathbf{H} = \Xi^\top \Sigma^{-1} \Xi, \quad (24)$$

with Σ the residual weights obtained following [25]. Using the full \mathbf{H} is misleading because it includes nuisance depths λ_j^n , often ill-conditioned under weak observations or low parallax, and prone to depressing some singular values. Hence, we marginalize depths via the Schur complement to obtain \mathbf{H}^* over the nine states to be estimated (gravity, velocity, accelerometer bias) and evaluate observability on this reduced matrix.

We then compute the SVD of $\mathbf{H}^* \in \mathbb{S}_+^9$ and define the singular-value ratio $\rho_j = \sigma_{\max}/\sigma_{\min}$, where σ_{\min} and σ_{\max} denote the smallest nonzero and largest singular values, respectively. To track stabilization as the data window grows, we monitor the relative change

$$\Delta\rho_j = \left| \frac{\rho_j - \rho_{j-1}}{\rho_{j-1}} \right|, \quad (25)$$

where large values indicate that observability is still changing, whereas consistently small values suggest that the Hessian has stabilized and the state is effectively observable. Once

$$\Delta\rho_j < \Delta\rho_{\text{th}}, \quad (\text{Full Observability Test}) \quad (26)$$

with $\Delta\rho_{\text{th}}$ a fixed threshold, we deem the system sufficiently observable and proceed to solve Eq. (20). Fig. 1 reports the relative overcost of the *Full Observability Test* with respect to the *Translation Observability Test*. The overcost of the *Full Observability Test* rises steadily with the window size: starting at roughly $\times 3$ -4 the cost of the *Translation Observability Test* for short windows, but exceeding $\times 15$ around ten frames. These results motivate the use of the parallax gate as the primary trigger and reserving the Hessian test as a final verifier.

VI. EXPERIMENTS

A. Experimental Setup

All experiments were conducted on a desktop PC equipped with an Intel Core i7-11700K (3.6 GHz, 64 GB RAM). Our method is implemented in C++, and nonlinear least-squares optimization is performed using Ceres [26]. Unless otherwise specified, all methods are executed on a single thread to ensure fair timing comparisons, and we report wall-clock times. Performance is evaluated in terms of the root mean squared error (RMSE), expressed in the corresponding physical units. In line with previous research, we use the publicly available EuRoC MAV benchmark [27], which comprises 11 sequences captured by a micro-aerial vehicle in two indoor environments: Machine Hall and Vicon Rooms. EuRoC provides synchronized stereo imagery (752 \times 480 at

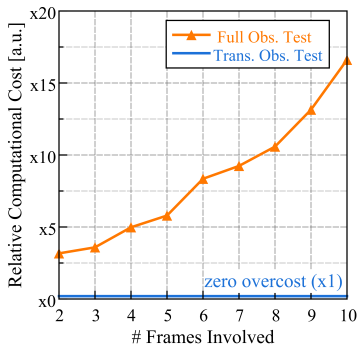


Fig. 1: **Relative computational costs of our observability tests.** Note the significantly higher cost of the full observability test, which motivates our proposal of a first stage assessing translational observability.

20 Hz) and inertial data at 200 Hz accompanied by accurate ground truth. The dataset spans a range of motion profiles (easy/medium/difficult) and exhibits variations in texture, illumination, and dynamics, making it a suitable testbed for evaluating initialization accuracy, robustness, and runtime under realistic conditions. We perform exhaustive initialization tests across all sequences in the EuRoC dataset. Following previous works [11], [14], we trigger initialization every 0.5 s (i.e., every 10 frames), yielding a total of 2248 independent initialization tests.

B. Closed-form gyroscope bias

Synthetic data: We conduct synthetic experiments in which the ground-truth relative rotations R_{ij} from EuRoC are progressively corrupted with zero-mean Gaussian noise, allowing us to isolate the effect of rotational uncertainty on the estimation accuracy of \mathbf{b}^g . We report de-aggregated per-sequence metrics to assess generalization over different motion patterns. As shown in Table II, in an ideal noise-free setup, nonlinear optimization yields the lowest errors, while our closed-form solutions perform only slightly worse. However, as the noise level increases (Tables III–V), the errors of our closed-form methods and the nonlinear baseline rapidly converge toward each other. In Table III, even for unrealistically small rotation errors below 0.01deg, the difference in \mathbf{b}^g error is already below 3%. For larger perturbations (Tables IV and V), the differences become negligible. These results indicate that, in practical scenarios with noisy relative rotation estimations, our closed-form solutions achieve a \mathbf{b}^g estimation accuracy comparable to that of nonlinear optimization. Note also that the differences among our approximations are negligible.

Real data: In this experiment, relative rotations R_{ij} are computed from image correspondences using C2P [28], with outliers removed via RANSAC. This setup emulates realistic conditions in which rotational inputs are derived from real visual data and are therefore affected by noise and matching inaccuracies. Across all initialization experiments, the average outlier ratio was approximately 0.15.

Seq.	Nonlin. Opt.	Closed-form solutions (ours)		
		Commutative	Avg.	Arithm. Avg.
MH01	0.000002	0.000299	0.000042	0.000315
MH02	0.000003	0.000303	0.000043	0.000329
MH03	0.000004	0.000444	0.000055	0.000486
MH04	0.000003	0.000327	0.000045	0.000338
MH05	0.000003	0.000275	0.000042	0.000283
V101	0.000003	0.000446	0.000052	0.000453
V102	0.000004	0.000947	0.000104	0.000965
V103	0.000007	0.001099	0.000123	0.001157
V201	0.000004	0.000439	0.000059	0.000463
V202	0.000004	0.000985	0.000109	0.001049
V203	0.000008	0.001384	0.000166	0.001552
Mean	0.000004	0.000631	0.000076	0.000672

TABLE II: **[Noise-free]** Gyroscope bias errors [rad/s] in EuRoC. We compare four different methods, including Nonlinear optimization (*Nonlin. Opt.*), commutative approximation, average approximation (*Avg.*) and arithmetic average approximation (*Arithm. Avg.*). Best per row in **bold**.

Seq.	Nonlin. Opt.	Closed-form solutions (ours)		
		Commutative	Avg.	Arithm. Avg.
MH01	0.004148	0.004166	0.004149	0.004182
MH02	0.004144	0.004144	0.004144	0.004185
MH03	0.004148	0.004169	0.004148	0.004189
MH04	0.004148	0.004147	0.004145	0.004145
MH05	0.004148	0.004161	0.004147	0.004170
V101	0.004148	0.004181	0.004147	0.004183
V102	0.004147	0.004350	0.004158	0.004353
V103	0.004147	0.004422	0.004163	0.004430
V201	0.004148	0.004181	0.004148	0.004180
V202	0.004149	0.004233	0.004144	0.004208
V203	0.003711	0.004116	0.003729	0.004132
Mean	0.004108	0.004206	0.004111	0.004214

TABLE III: **[Noise = 0.006 deg]** Results of gyroscope bias estimation error [rad/s] in EuRoC dataset. We compare four different methods, including Nonlinear optimization (*Nonlin. Opt.*), commutative approximation, average approximation (*Avg.*) and arithmetic average approximation (*Arithm. Avg.*). Best per row in **bold**.

Seq.	Nonlin. Opt.	Closed-form solutions (ours)		
		Commutative	Avg.	Arithm. Avg.
MH01	0.020741	0.020745	0.020741	0.020760
MH02	0.020740	0.020723	0.020736	0.020763
MH03	0.020741	0.020733	0.020740	0.020738
MH04	0.020741	0.020724	0.020738	0.020720
MH05	0.020741	0.020741	0.020739	0.020748
V101	0.020741	0.020747	0.020739	0.020747
V102	0.020740	0.020844	0.020750	0.020835
V103	0.020740	0.020882	0.020754	0.020861
V201	0.020741	0.020747	0.020740	0.020742
V202	0.020742	0.020706	0.020736	0.020654
V203	0.018558	0.018695	0.018571	0.018618
Mean	0.020542	0.020571	0.020544	0.020562

TABLE IV: **[Noise = 0.03 deg]** Results of gyroscope bias estimation error [rad/s] in EuRoC dataset. We compare four different methods, including Nonlinear optimization (*Nonlin. Opt.*), commutative approximation, average approximation (*Avg.*) and arithmetic average approximation (*Arithm. Avg.*). Best per row in **bold**.

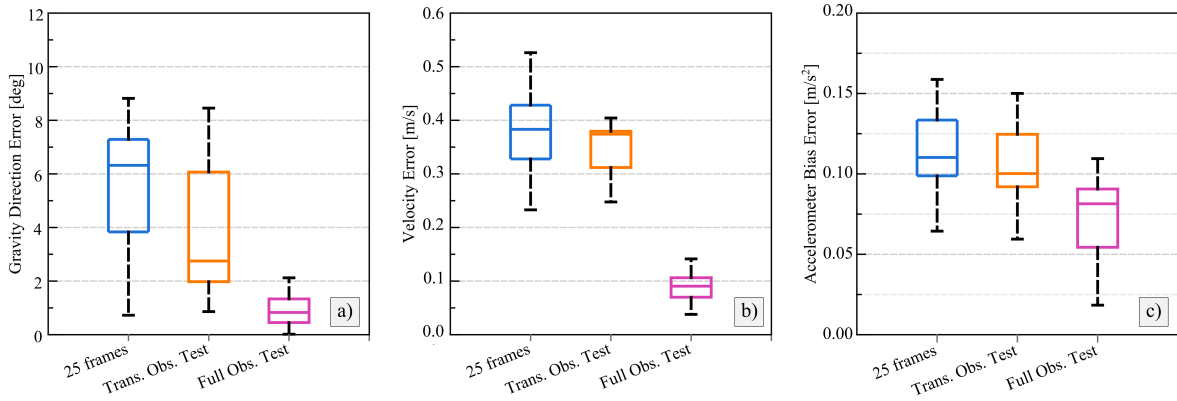


Fig. 2: **Initialization accuracy vs. activation policy.** We trigger closed-form initialization at three instants: (i) after a fixed 25-frame window (≈ 1.25 s); (ii) when the first observability criteria (*Translation Observability Test*) is satisfied; and (iii) the second observability criteria (*Full Observability Test*) is satisfied. Panels report RMSE distributions in (a) gravity direction, (b) velocity, and (c) accelerometer bias. The *Translation Observability Test* already improves initialization accuracy, while the *Full Observability Test* yields the best overall performance.

Seq.	Nonlin. Opt.	Closed-form solutions (ours)		
		Commutative	Avg.	Arithm. Avg.
MH01	0.041481	0.041484	0.041482	0.041498
MH02	0.041481	0.041462	0.041476	0.041502
MH03	0.041481	0.041470	0.041481	0.041471
MH04	0.041481	0.041462	0.041478	0.041458
MH05	0.041481	0.041480	0.041479	0.041486
V101	0.041481	0.041484	0.041480	0.041484
V102	0.041481	0.041571	0.041490	0.041561
V103	0.041481	0.041605	0.041495	0.041581
V201	0.041481	0.041484	0.041481	0.041478
V202	0.041483	0.041432	0.041477	0.041377
V203	0.037116	0.037212	0.037129	0.037109
Mean	0.041084	0.041104	0.041086	0.041091

TABLE V: [**Noise = 0.06 deg**] Results of gyroscope bias estimation error [rad/s] in EuRoC dataset. We compare four different methods, including Nonlinear optimization (*Nonlin. Opt.*), commutative approximation, average approximation (*Avg.*) and arithmetic average approximation (*Arithm. Avg.*). Best per row in **bold**.

Table VI summarizes the average gyroscope bias estimation errors across all EuRoC sequences, for our closed-form solutions and nonlinear optimization. Table VII reports the mean and standard deviation of the execution time for gyroscope bias estimation under the four aforementioned strategies. Relative to the nonlinear baseline (3.687 ms), the *Commutative* approximation reduces runtime by $\sim 97.5\%$ ($39\times$, ~ 1.6 orders of magnitude), the *Avg.* approximation by $\sim 99.3\%$ ($147\times$, ~ 2.2 orders), and the *Arithm. Avg.* approximation by $\sim 99.5\%$ ($194\times$, ~ 2.3 orders). This validates the computational advantage of our approximations for the initialization of \mathbf{b}^g .

As a summary, note how under realistic conditions all our methods achieve comparable accuracy, with noticeable differences only in the unrealistic noise-free case. The errors coming from feature matching are significantly higher than

Seq.	Nonlin. Opt.	Closed-form solutions (ours)		
		Commutative	Avg.	Arithm. Avg.
MH01	0.030048	0.030020	0.030046	0.030028
MH02	0.033075	0.033052	0.033072	0.033064
MH03	0.029123	0.029152	0.029126	0.029161
MH04	0.045381	0.045410	0.045384	0.045392
MH05	0.038635	0.038620	0.038633	0.038622
V101	0.044986	0.044941	0.044980	0.044946
V102	0.090967	0.090799	0.090948	0.090825
V103	0.351947	0.351923	0.351939	0.351934
V201	0.048773	0.048756	0.048769	0.048765
V202	0.057977	0.058014	0.057978	0.058041
V203	0.122305	0.122289	0.122303	0.122330
Mean	0.081202	0.081180	0.081198	0.081192

TABLE VI: [**Realistic**] Results of gyroscope bias estimation error [rad/s] in EuRoC dataset. We compare four different methods, including Nonlinear optimization (*Nonlin. Opt.*), commutative approximation, average approximation (*Avg.*) and arithmetic average approximation (*Arithm. Avg.*). Best per row in **bold**.

that of our approximations, which are negligible in practice. The accuracy of our three proposed approximations is similar, while *Arithm. Avg.* is the most efficient, and hence should be the preferred one for implementation.

C. Full state Initialization

Evaluation of Triggering strategies: To assess our observability-driven initialization policy, we compared three different activation strategies: (i) a fixed-time policy after 25 frames (≈ 1.25 s), (ii) activation when the first observability criteria (*Translation Observability Test*) is satisfied, and (iii) activation when the second observability criteria (*Full Observability Test*) is satisfied.

Fig. 2 reports the results of this experiment and highlights the advantages of our two-stage strategy over a naive fixed-window policy. A fixed activation after 25 frames yields noticeably larger and more dispersed errors, particularly in

Method	Mean [μ s]	Std dev. [μ s]
Nonlinear optimization	3687	275
Commutative approximation (ours)	94	6
Avg. approximation (ours)	25	1
Arithm. Avg approximation (ours)	19	1

TABLE VII: **Gyroscope bias initialization runtime on EuRoC.** The commutative and average-velocity approximations achieve up to two orders of magnitude speed-up compared to the nonlinear optimization baseline.

the gravity estimate, as no guarantees exist on the state observability in the chosen interval. By contrast, activating the closed-form full solution at the first *Translation Observability Test* already achieves a clear reduction in error. And even greater improvements are obtained when monitoring the Hessian and postponing activation until the *Full Observability Test* is satisfied, which consistently yields the lowest errors across all estimated state variables. These results confirm that our observability-driven criterion not only enables faster initialization than fixed-time approaches, but also provides more accurate and reliable estimates than a fixed-window strategy.

Comparison against baselines: We use as baselines the tightly-coupled version of DRT (denoted as DRT-tight) [14], VINS-Mono initialization (denoted as VINS-Mono) [29], and the analytical-solution [30] which is an improved work of the ORB-SLAM3 initialization [11] (denoted as AS-MLE). Table VIII summarizes per-sequence initialization accuracy on EuRoC, comparing our approach against AS-MLE, VINS-Mono, and DRT-tight. Averaging across sequences, our method attains the lowest velocity RMSE (0.09 m/s) and gravity-direction error (0.90 deg), outperforming DRT-tight (0.11 m/s, 1.03 deg), VINS-Mono (0.11 m/s, 1.47 deg), and AS-MLE (0.17 m/s, 2.66 deg). The per-row highlights indicate that our initializer is best or second-best in the majority of sequences for both velocity and gravity, with isolated cases where DRT-tight remains competitive (e.g., V102 gravity). Overall, these results show that a closed-form, structure-free design yields consistently stronger velocity and gravity estimates at the end of initialization, providing a more reliable starting point for subsequent optimization. For the accelerometer bias, our method also achieves the lowest average RMSE (0.084 m/s²), improving over AS-MLE and VINS-Mono. This confirms that bias effects are well captured during initialization. As noted by the authors, DRT-tight does not model accelerometer bias in its translation constraints, hence the missing entries in Table VIII.

Running time evaluation: We evaluate our overall initialization runtime against representative baselines on the EuRoC dataset. In Table IX the full state initialization time is broken down by modules. Our method does not require 3D structure during initialization; therefore, we only include the cost of gyroscope bias estimation and the velocity-gravity solver. For a fair comparison with methods that rely on structure, we additionally report an optional “Point Tri.” stage executed after initialization. Our total initialization (0.96 ms)

is 96.9% lower than AS-MLE (30.54 ms; 31.8 \times , \sim 1.5 orders), 96.9% lower than VINS-Mono (30.94 ms; 32.2 \times , \sim 1.5 orders), and 81.5% lower than DRT-tight (5.18 ms; 5.4 \times , \sim 0.73 orders). At the module level, gyroscope-bias estimation is reduced by 86.7% vs AS-MLE (7.5 \times), 95.5% vs VINS-Mono (22 \times), and 99.0% vs DRT-tight (97.5 \times). Our closed-form velocity-gravity solver is faster than DRT-tight by 81.5% (5.4 \times), while being 3.7–6.5 \times slower than AS-MLE/VINS-Mono (which leverage prebuilt structure). Notably, our pipeline avoids the SfM stage (\approx 30 ms in AS-MLE/VINS-Mono), which dominates their cost; if reporting *core-only* initialization (bias + vel. grav.), our time is 0.54 ms, i.e., 98.2% lower than AS-MLE (56.6 \times , \sim 1.75 orders).

Initialization times: Table X compares the initialization windows used by the baselines and our method. Prior approaches require temporal windows of roughly two seconds on average, either fixed or adaptively selected. In contrast, our two-stage criterion achieves reliable initialization with an adaptive window averaging only half a second.

VII. CONCLUSIONS

In this work, we introduced a closed-form initialization that recovers the full visual-inertial state without iterative solvers. By exploiting small-rotation and constant-velocity approximations, the method preserves the essential couplings between motion and inertial measurements while remaining analytically compact. A central ingredient is our fast approximation for gyroscope-bias estimation, which replaces costly optimization with a lightweight solve and enables its immediate, robust start-up. Across all EuRoC sequences, our method reduces the visual-inertial initialization errors of relevant baselines by 10 – 20%, reduces initialization windows by 4 \times and computation times by 5 \times . Importantly, our solutions are also algebraically simpler. We believe our closed-form perspective offers a practical alternative for resource-constrained platforms and a strong foundation for future extensions within modern visual-inertial pipelines.

REFERENCES

- [1] T. Qin, P. Li, and S. Shen, “Vins-mono: A robust and versatile monocular visual-inertial state estimator,” *IEEE transactions on robotics*, vol. 34, no. 4, pp. 1004–1020, 2018.
- [2] C. Campos, R. Elvira, J. J. G. Rodríguez, J. M. Montiel, and J. D. Tardós, “Orb-slam3: An accurate open-source library for visual, visual-inertial, and multimap slam,” *IEEE transactions on robotics*, vol. 37, no. 6, pp. 1874–1890, 2021.
- [3] S. Boche, J. Jung, S. B. Laina, and S. Leutenegger, “Okvis2-x: Open keyframe-based visual-inertial slam configurable with dense depth or lidar, and gnss,” *IEEE Transactions on Robotics*, 2025.
- [4] L. Carlone and A. Censi, “From angular manifolds to the integer lattice: Guaranteed orientation estimation with application to pose graph optimization,” *IEEE Transactions on Robotics*, vol. 30, no. 2, pp. 475–492, 2014.
- [5] L. Carlone, R. Tron, K. Daniilidis, and F. Dellaert, “Initialization techniques for 3d slam: A survey on rotation estimation and its use in pose graph optimization,” in *2015 IEEE international conference on robotics and automation (ICRA)*. IEEE, 2015, pp. 4597–4604.
- [6] A. Martinelli, “Vision and imu data fusion: Closed-form solutions for attitude, speed, absolute scale, and bias determination,” *IEEE Transactions on Robotics*, vol. 28, no. 1, pp. 44–60, 2011.
- [7] —, “Closed-form solution of visual-inertial structure from motion,” *International journal of computer vision*, vol. 106, no. 2, pp. 138–152, 2014.

Seq.	Velocity Error [m/s]				Gravity Direction Error [deg]				Accelerometer Bias Error [m/s ²]			
	AS-MLE	VINS-Mono	DRT-tight	Ours	AS-MLE	VINS-Mono	DRT-tight	Ours	AS-MLE	VINS-Mono	DRT-tight	Ours
MH01	0.11	0.08	0.11	<u>0.10</u>	1.64	1.17	<u>1.00</u>	0.87	0.093	<u>0.092</u>	–	0.088
MH02	<u>0.09</u>	0.08	0.11	<u>0.09</u>	1.36	1.11	<u>0.97</u>	0.65	<u>0.092</u>	0.093	–	0.091
MH03	0.30	0.19	<u>0.14</u>	0.09	3.06	<u>1.57</u>	0.96	0.96	0.080	0.081	–	0.080
MH04	0.25	<u>0.14</u>	0.19	0.11	1.87	1.23	<u>0.99</u>	0.84	<u>0.087</u>	0.088	–	0.086
MH05	0.25	<u>0.17</u>	0.22	0.13	2.61	1.42	<u>0.99</u>	0.83	0.084	0.081	–	0.081
V101	<u>0.07</u>	0.06	<u>0.07</u>	<u>0.07</u>	3.37	–	<u>0.99</u>	0.89	<u>0.316</u>	0.319	–	0.128
V102	0.24	0.11	<u>0.06</u>	0.05	5.57	2.60	0.79	<u>1.09</u>	0.082	<u>0.081</u>	–	0.078
V103	–	–	0.11	<u>0.12</u>	–	–	<u>1.48</u>	0.87	<u>0.115</u>	0.116	–	0.094
V201	0.08	<u>0.07</u>	0.08	0.06	1.79	1.43	<u>1.15</u>	1.06	0.085	<u>0.083</u>	–	0.082
V202	0.13	<u>0.08</u>	0.06	<u>0.07</u>	2.68	1.26	0.84	<u>0.94</u>	<u>0.055</u>	0.056	–	0.052
V203	–	–	<u>0.09</u>	0.08	–	–	<u>1.17</u>	0.92	0.053	0.053	–	0.062
Mean	0.17	<u>0.11</u>	<u>0.11</u>	0.09	2.66	1.47	<u>1.03</u>	0.90	0.104	0.104	–	0.084

TABLE VIII: Per-sequence initialization errors on EuRoC (attempts every 0.5s). Velocity, gravity direction and accelerometer bias errors for AS-MLE, VINS-Mono, DRT-tight, and ours. Best per row in **bold**, second-best underlined.

Module	AS-MLE	VINS-Mono	DRT-tight	Ours
SfM	30.30	30.35	–	–
\mathbf{b}^g Est.	0.15	0.44	1.95	0.02
Vel. & Grav. Est.	0.08	0.14	2.81	0.52
Point Tri.	0.01	0.01	0.42	0.42
Total	30.54	30.94	5.18	0.96

TABLE IX: Average initialization cost [ms] on EuRoC. Runtime breakdown and comparison against baselines.

Method	Initialization time [s]	Adaptive?
Campos et al. [10]	2.16 ± 0.01	✓
He et al. [14]	2.50	✗
Ours	0.48 ± 0.27	✓

TABLE X: Initialization window length and adaptivity. Whereas baselines rely on fixed windows and long initialization windows, our two-stage criterion reduces initialization delays 4×.

- [8] J. Kaiser, A. Martinelli, F. Fontana, and D. Scaramuzza, “Simultaneous state initialization and gyroscope bias calibration in visual inertial aided navigation,” *IEEE Robotics and Automation Letters*, vol. 2, no. 1, pp. 18–25, 2016.
- [9] J. Domínguez-Conti, J. Yin, Y. Alami, and J. Civera, “Visual-inertial slam initialization: A general linear formulation and a gravity-observing non-linear optimization,” in *2018 IEEE International Symposium on Mixed and Augmented Reality (ISMAR)*. IEEE, 2018, pp. 37–45.
- [10] C. Campos, J. M. Montiel, and J. D. Tardós, “Fast and robust initialization for visual-inertial slam,” in *2019 International Conference on Robotics and Automation (ICRA)*. IEEE, 2019, pp. 1288–1294.
- [11] —, “Inertial-only optimization for visual-inertial initialization,” in *2020 IEEE International Conference on Robotics and Automation (ICRA)*. IEEE, 2020, pp. 51–57.
- [12] S. H. Lee and J. Civera, “Rotation-only bundle adjustment,” in *Proceedings of the IEEE/CVF Conference on Computer Vision and Pattern Recognition*, 2021, pp. 424–433.
- [13] A. Concha, M. Burri, J. Briales, C. Forster, and L. Oth, “Instant visual odometry initialization for mobile ar,” *IEEE Transactions on Visualization and Computer Graphics*, vol. 27, no. 11, pp. 4226–4235, 2021.
- [14] Y. He, B. Xu, Z. Ouyang, and H. Li, “A rotation-translation-decoupled solution for robust and efficient visual-inertial initialization,” in *Proceedings of the IEEE/CVF Conference on Computer Vision and Pattern Recognition*, 2023, pp. 739–748.
- [15] R. Wang, X. Qian, X. Gao, and L. Chen, “Edi: An error-state kalman filter based disjoint initialization framework for visual-inertial slam,” *IEEE Robotics and Automation Letters*, vol. 8, no. 9, pp. 5905–5912, 2023.
- [16] G. D. Evangelidis and B. Micušík, “Revisiting visual-inertial structure-from-motion for odometry and slam initialization,” in *2020 IEEE International Conference on Robotics and Automation (ICRA)*. IEEE, 2020, pp. 5172–5178.
- [17] L. Kneip and S. Lynen, “Direct optimization of frame-to-frame rotation,” in *Proceedings of the IEEE International Conference on Computer Vision*, 2013, pp. 2352–2359.
- [18] J. Oliensis, “Exact two-image structure from motion,” *IEEE Transactions on Pattern Analysis and Machine Intelligence*, vol. 24, no. 12, pp. 1618–1633, 2002.
- [19] S. H. Lee and J. Civera, “Closed-form optimal two-view triangulation based on angular errors,” in *Proceedings of the IEEE/CVF International Conference on Computer Vision*, 2019, pp. 2681–2689.
- [20] F. Yu and D. Gallup, “3d reconstruction from accidental motion,” in *Proceedings of the IEEE Conference on Computer Vision and Pattern Recognition*, 2014, pp. 3986–3993.
- [21] J. Ventura, C. Arth, and V. Lepetit, “Approximated relative pose solvers for efficient camera motion estimation,” in *European Conference on Computer Vision*. Springer, 2014, pp. 180–193.
- [22] C. Forster, L. Carlone, F. Dellaert, and D. Scaramuzza, “On-manifold preintegration for real-time visual-inertial odometry,” *IEEE Transactions on Robotics*, vol. 33, no. 1, pp. 1–21, 2017.
- [23] A. Fontan, L. Oliva, J. Civera, and R. Triebel, “Model for multi-view residual covariances based on perspective deformation,” *IEEE Robotics and Automation Letters*, vol. 7, no. 2, pp. 1960–1967, 2022.
- [24] S. Cerezo and J. Civera, “Gnss-inertial state initialization by distance residuals,” *arXiv preprint arXiv:2506.11534*, 2025.
- [25] —, “Camera motion estimation from rgb-d-inertial scene flow,” in *2024 IEEE/CVF Conference on Computer Vision and Pattern Recognition Workshops (CVPRW)*, 2024, pp. 841–849.
- [26] S. Agarwal, K. Mierle, and T. C. S. Team, “Ceres Solver,” 10 2023. [Online]. Available: <https://github.com/ceres-solver/ceres-solver>
- [27] M. Burri, J. Nikolic, P. Gohl, T. Schneider, J. Rehder, S. Omari, M. W. Achtelik, and R. Siegwart, “The euroc micro aerial vehicle datasets,” *The International Journal of Robotics Research*, 2016.
- [28] J. Tirado-Garín and J. Civera, “From correspondences to pose: Non-minimal certifiably optimal relative pose without disambiguation,” *CVPR*, 2024.
- [29] T. Qin, P. Li, and S. Shen, “Vins-mono: A robust and versatile monocular visual-inertial state estimator,” *IEEE Transactions on Robotics*, vol. 34, no. 4, pp. 1004–1020, 2018.
- [30] D. Zuniga-Noël, F.-A. Moreno, and J. Gonzalez-Jimenez, “An analytical solution to the imu initialization problem for visual-inertial systems,” *IEEE Robotics and Automation Letters*, vol. 6, no. 3, pp. 6116–6122, 2021.